

OBSERVATIONAL SIGNATURES OF CLOUD-CLOUD COLLISION IN THE EXTENDED STAR-FORMING REGION S235

L. K. DEWANGAN¹ AND D. K. OJHA²

ABSTRACT

We present a multi-wavelength data analysis of the extended star-forming region S235 (hereafter E-S235), where two molecular clouds are present. In E-S235, using the ¹²CO (1-0) and ¹³CO (1-0) line data, a molecular cloud linked with the site “S235main” is traced in a velocity range [−24, −18] km s^{−1}, while the other one containing the sites S235A, S235B, and S235C (hereafter “S235ABC”) is depicted in a velocity range [−18, −13] km s^{−1}. In the velocity space, these two clouds are separated by ∼4 km s^{−1}, and are interconnected by a lower intensity intermediate velocity emission, tracing a broad bridge feature. In the velocity channel maps, a possible complementary molecular pair at [−21, −20] km s^{−1} and [−16, −15] km s^{−1} is also evident. The sites, “S235ABC”, East 1, and South-West are spatially seen in the interface of two clouds. Together, these observed features are consistent with the predictions of numerical models of the cloud-cloud collision (CCC) process, favoring the onset of the CCC in E-S235 about 0.5 Myr ago. Deep UKIDSS near-infrared photometric analysis of point-like sources reveals significant clustering of young stellar populations toward the sites located at the junction, and the “S235main”. The sites, “S235ABC” harbor young compact H II regions having dynamical ages of ∼0.06–0.22 Myr, and these sites (including South-West and East 1) also contain dust clumps (having $M_{clump} \sim 40$ to 635 M_{\odot}). Our observational findings suggest that the star formation activities (including massive stars) appear to be influenced by the CCC mechanism at the junction.

Subject headings: dust, extinction – H II regions – ISM: clouds – ISM: individual objects (S235) – stars: formation – stars: pre-main sequence

1. INTRODUCTION

The young stellar populations can be formed spontaneously throughout a given molecular cloud (e.g., Preibisch & Zinnecker 2007). On the other hand, the collapse and star formation can be influenced by some external agents such as the expansion of H II regions (e.g., Elmegreen & Lada 1977; Elmegreen 1998) and the cloud-cloud collision (CCC) process (e.g., Habe & Ohta 1992; Anathpindika 2010; Inoue & Fukui 2013; Takahira et al. 2014). In recent years, the study of the triggered star formation through the CCC process is an interesting and important issue in the star formation research (e.g., Torii et al. 2017a, and references therein). It has also been suggested that the CCC process can form massive OB stars and young stellar clusters at the junction of molecular clouds (e.g., Habe & Ohta 1992; Furukawa et al. 2009; Ohama et al. 2010; Inoue & Fukui 2013; Takahira et al. 2014; Fukui et al. 2014, 2016; Torii et al. 2015, 2017a; Haworth et al. 2015a,b; Dewangan 2017). In hydrodynamical numerical simulations, it has been shown that the CCC triggers the birth of dense clumps/cores in the shock-compressed interface, and these dense clumps/cores can further lead to the formation of a new generation of stars (Habe & Ohta (1992); Anathpindika (2010), and also see Figure 1 in Torii et al. (2017a)). Furthermore, Takahira et al. (2014) studied the formation and evolution of pre-stellar gas cores in

the collision of non-identical clouds with Bonner-Ebert profiles using hydrodynamical simulations. Recent magnetohydrodynamical numerical simulations have demonstrated that the CCC process can enable the formation of the massive clumps in the collisional-compressed layer (Inoue & Fukui 2013). More recently, based on the comparisons between observations and existing models, Torii et al. (2017a) reported the characteristic features of the CCC, such as the complementary distribution of the two colliding clouds, the bridge feature at the intermediate velocity range, and its flattened CO spectrum. These features are promising to obtain convincing evidences to support the idea that two molecular components are interacting with each other in a given star-forming complex. Torii et al. (2017a) also provided a table of promising star-forming sites where the star formation process could be explained by the CCC process. However, the investigation of observational signatures of star formation (including massive stars) via the CCC mechanism is still rare and very challenging.

The extended star-forming region S235 (hereafter E-S235) is part of the giant molecular cloud G174+2.5 in the Perseus Spiral Arm (e.g. Heyer et al. 1996) and is a very well studied site using the multi-wavelength data covering from optical, near-infrared (NIR) to radio wavelengths (e.g., Georgelin et al. 1973; Israel & Felli 1978; Evans & Blair 1981; Evans et al. 1981; Nordh et al. 1984; Brand & Blitz 1993; Felli et al. 1997, 2004, 2006; Allen et al. 2005; Kirsanova et al. 2008, 2014; Boley et al. 2009; Dewangan & Anandarao 2011; Camargo et al. 2011; Kang et al. 2012; Chavarría et al. 2014; Navarete et al. 2015; Foster & Brunt 2015; Burns et al. 2015, 2016; Ladeyschikov et al. 2016; Bieging et al. 2016; Dewan-

lokeshd@prl.res.in

¹ Physical Research Laboratory, Navrangpura, Ahmedabad - 380 009, India.² Department of Astronomy and Astrophysics, Tata Institute of Fundamental Research, Homi Bhabha Road, Mumbai 400 005, India.

gan et al. 2016, etc.). Located at a distance of 1.8 kpc (Evans & Blair 1981), E-S235 is a nearby star-forming region that consists of previously known star-forming sites, “S235 complex (or S235main)”, S235A, S235B, and S235C (or “S235ABC”) (see Figure 1 in Dewangan & Anandarao (2011) (hereafter Paper I) and also in Kirsanova et al. (2014)). In E-S235, Evans & Blair (1981) found two velocity components at -20 km s^{-1} (linked with “S235main”) and -17 km s^{-1} (containing the sites “S235ABC”). This implies that the molecular gas linked with the sites “S235ABC” is redshifted with respect to the S235main molecular cloud. Furthermore, using ^{13}CO (1–0) line data, Kirsanova et al. (2008) traced three molecular gas components (i.e., $-18 \text{ km s}^{-1} < V_{lsr} < -15 \text{ km s}^{-1}$ (red), $-21 \text{ km s}^{-1} < V_{lsr} < -18 \text{ km s}^{-1}$ (central), and $-25 \text{ km s}^{-1} < V_{lsr} < -21 \text{ km s}^{-1}$ (blue)) in the direction of E-S235. An extended H II region linked with the “S235main” is ionized by a single massive star BD+35°1201 of O9.5V type (Georgelin et al. 1973), while the sites, S235A, S235B, and S235C are associated with compact H II regions, which are mainly excited by B1V–B0.5V stars (see Table 1 in Bieging et al. 2016, and references therein). The existing observations and interpretations of E-S235 suggest that the H II regions associated with the “S235main” and the “S235ABC” are interacting with their surrounding molecular clouds. Photometric analysis of point-like sources indicated the intense star formation activities in these molecular clouds (Kirsanova et al. 2008; Dewangan & Anandarao 2011; Chavarría et al. 2014; Dewangan et al. 2016; Bieging et al. 2016). Furthermore, these sites have been cited as promising regions of triggered star formation by the expanding H II regions (Kirsanova et al. 2008, 2014; Camargo et al. 2011; Bieging et al. 2016). Dewangan et al. (2016) (hereafter Paper II) performed a multi-wavelength study of star formation activity in the “S235main” and found that at least five subregions (i.e. Central E, East 2, North, North-West, and Central W) (having $A_V > 8$ mag) appear to be nearly regularly spaced along the sphere-like shell surrounding the ionized emission. These results have also been seen in the molecular and dust continuum maps. They concluded that the “S235main” can be considered as a promising nearby site of triggered star formation. Furthermore, in E-S235, they also found an almost broad bridge feature in the velocity space and suggested a possibility of the applicability of the CCC process. They suggested that the CCC process might have influenced the star formation activity at the interface between the S235main molecular cloud and the “S235ABC” molecular cloud (i.e. South-West subregion). In Paper II, the analysis was focused mainly on the “S235main” site. Hence, a detailed study of the CCC process concerning the formation of young stellar clusters and massive stars in E-S235 is yet to be carried out.

To explore the CCC process in E-S235, we have used the narrow-band H α image from the Isaac Newton Telescope Photometric H α Survey of the Northern Galactic Plane (IPHAS; Drew et al. 2005), NIR data from the UKIDSS Galactic Plane Survey (GPS; Lawrence et al. 2007), radio continuum data at 610 MHz from the Giant Metre-wave Radio Telescope (GMRT) database, and dust continuum 1.1 mm data (Aguirre et al. 2011; Ginsburg et al. 2013) from the Bolocam Galactic Plane Sur-

vey (BGPS). Additionally, several published data (i.e. *Spitzer* NIR and mid-infrared (MIR) data (from Dewangan & Anandarao 2011), and the Five College Radio Astronomy Observatory (FCRAO) ^{12}CO (1-0) and ^{13}CO (1-0) line data (Heyer et al. 1998; Brunt 2004)) were also utilized.

This paper is structured as follows. In Section 2, we discuss the data selection. The results of our extensive multi-wavelength data analysis are presented in Section 3. The implications of our findings concerning the star formation are discussed in Section 4. Finally, the results are summarized and concluded in Section 5.

2. DATA AND ANALYSIS

In this work, we have selected a region of $\sim 24' \times 24'$ (or $\sim 12.5 \text{ pc} \times 12.5 \text{ pc}$ at a distance of 1.8 kpc) (central coordinates: $\alpha_{2000} = 05^{\text{h}}41^{\text{m}}02^{\text{s}}$, $\delta_{2000} = +35^{\circ}47'25''$) containing E-S235. In the following, we provide a brief description of the adopted multi-frequency data-sets.

2.1. Narrow-band H α image

Narrow-band H α image at $0.6563 \mu\text{m}$ was retrieved from the IPHAS database. The survey was carried out using the Wide-Field Camera (WFC) at the 2.5-m Isaac Newton Telescope, located at La Palma. The WFC contains four $4\text{k} \times 2\text{k}$ CCDs, in an L-shape configuration. The pixel scale is $0''.33$ and the instantaneous field of view is about 0.3 square degrees. More details about the IPHAS can be found in Drew et al. (2005).

2.2. Near-infrared data

We analyzed the deep NIR photometric *HK* magnitudes of point sources extracted from the UKIDSS GPS sixth archival data release (UKIDSSDR6plus) and Two Micron All Sky Survey (2MASS; Skrutskie et al. 2006). The UKIDSS observations (resolution $\sim 0''.8$) were performed with the WFCAM mounted on the United Kingdom Infra-Red Telescope. 2MASS photometric data were utilized to calibrate the final fluxes. In this work, we extracted only a reliable NIR photometric catalog. More information about the selection procedures of the GPS photometry can be found in Dewangan et al. (2015). Our resultant GPS catalog consists of point sources fainter than $H = 12.3$ and $K = 11.4$ mag to avoid saturation. In our final catalog, the magnitudes of the saturated bright sources were obtained from the 2MASS catalog.

Additionally, we also obtained *Spitzer* $3.6 \mu\text{m}$ image from Paper I.

2.3. Dust continuum 1.1 mm data

Bolocam 1.1 mm image and Bolocam source catalog (v2.1) at 1.1 mm were extracted from the BGPS. The effective full width at half maximum (FWHM) of the 1.1 mm map is $\sim 33''$.

2.4. Radio continuum data

The 610 MHz continuum data were obtained from the GMRT archive and were observed on 18–19 June 2005 (Project Code: 08SKG01). The data reduction was performed using AIPS software, in a manner similar to that highlighted in Mallick et al. (2013). Since the S235 complex was distant from the center of the observed field,

the primary beam correction for 610 MHz was also done, using the AIPS PBCOR task and parameters from the GMRT manual¹. The synthesized beam size of the final 610 MHz map is $\sim 48'' \times 44''.2$ (also see Paper II).

2.5. Molecular CO line data

In E-S235, we probed the molecular gas content using the FCRAO ^{12}CO ($J=1-0$) and ^{13}CO ($J=1-0$) line data. The FCRAO beam sizes are $45''$ and $46''$ for ^{12}CO and ^{13}CO , respectively. The observations of E-S235 were made as part of the Extended Outer Galaxy Survey (E-OGS, Brunt 2004), that extends the coverage of the FCRAO Outer Galaxy Survey (OGS, Heyer et al. 1998) to Galactic longitude $l = 193^\circ$, over a latitude range of $-3^\circ.5 \leq b \leq +5^\circ.5$. However, the data cubes of E-S235 were further re-processed and a document describing the re-processing data methods is given in Brunt (2004) (also Brunt C.M. et al.; in preparation). These ^{13}CO data cubes were collected from M. Heyer and C. Brunt (through private communication). The FCRAO ^{13}CO ($J=1-0$) line data were also used in Paper II.

3. RESULTS

In this section, we present a multi-wavelength analysis of E-S235 to understand the ongoing physical processes operating in this target region.

3.1. Kinematics of molecular gas in E-S235

The study of molecular gas in a given star-forming complex can help to trace the physical association of different subregions. As mentioned earlier, two velocity components (at -20 and -17 km s⁻¹) are seen in the direction of E-S235 (Evans & Blair 1981). To explore the spatial distribution of molecular gas in E-S235, we present ^{12}CO ($J=1-0$) and ^{13}CO ($J=1-0$) velocity channel maps at different velocities covering a range from -24 to -12 km s⁻¹ in steps of 1 km s⁻¹ in Figures 1 and 2, respectively. The analysis of channel maps of both ^{12}CO and ^{13}CO emission reveals that the molecular cloud associated with the site “S235main” is traced in a velocity range of -23 to -18 km s⁻¹, while the molecular cloud linked with the sites “S235ABC” is depicted in a velocity range of -18 to -13 km s⁻¹. Together, our analysis is in agreement with the previously reported fact that the S235main molecular cloud is blueshifted with respect to the molecular cloud harboring the sites “S235ABC”. To further examine the velocity field and kinematical structure of the molecular gas in E-S235, using the ^{12}CO line data, we present the integrated intensity map and the position-velocity maps in Figure 3. In Figure 3a, the ^{12}CO emission is integrated over -24 to -13 km s⁻¹, tracing the gas distribution toward the sites, “S235main” and “S235ABC”. In Figures 3b and 3d, we present the position-velocity diagrams of ^{12}CO emission, tracing two molecular components as well as noticeable velocity gradients. In both the position-velocity maps, a redshifted molecular component (velocity peak at ~ -16.5 km s⁻¹) and a blueshifted component (velocity peak at ~ -20.5 km s⁻¹) are evident which are consistent with those observed in the channel maps of ^{12}CO emission. This implies that these peaks are separated by ~ 4 km s⁻¹. Furthermore, in Figure 3b, we find that these two velocity

peaks are interconnected by a lower intensity intermediate velocity emission, suggesting the presence of a broad bridge feature. In Figure 3c, we present the spatial distribution of ^{12}CO gas associated with the redshifted and the blueshifted molecular components within E-S235.

Using the ^{13}CO line data, we also show the integrated intensity map and the position-velocity maps in Figure 4. Figure 4a shows the ^{13}CO intensity map integrated over -24 to -13 km s⁻¹. Figures 4b and 4d present the position-velocity diagrams of ^{13}CO emission, depicting also two molecular components as well as the broad bridge feature. We have found that the bridge feature is more noticeable in the velocity space of ^{12}CO compared to ^{13}CO data. Note that in Paper II, only the declination-velocity map of ^{13}CO related to E-S235 was discussed. In Paper II, the presence of an expanding H II region was reported in “S235main”, on the basis of the detection of arc or ring-like features in the velocity space. Hence, in this work, we do not focus on these features seen in the velocity space. Figure 4c presents the spatial distribution of ^{13}CO gas linked with the blueshifted and the redshifted molecular components within E-S235. The distribution of ^{12}CO and ^{13}CO gas associated with both the clouds is spatially seen toward the sites, “S235ABC” and a few subregions located in the East and South-West with respect to the location of the O9.5V star (BD+35^o 1201) (see Figures 3c and 4c). It implies the presence of junction/intersection zones in both the space and velocity between two molecular clouds. To further explore the boundaries of these two clouds, we present ^{12}CO and ^{13}CO first moment maps in Figures 5a and 5b, respectively. These maps allow to reveal the V_{lsr} of the peak emission at each grid point and are measure of the intensity-weighted mean velocity of the emitting gas. These maps clearly trace two distinct molecular clouds and also depict their boundaries in E-S235. Figures 5c and 5d show maps of ^{12}CO and ^{13}CO velocity dispersions (δV) (i.e. the second-order moment), enabling to infer the line width at each pixel. A large dispersion may be explained by a broad single velocity component and/or may indicate the presence of two or more narrow components with different velocities along one line of sight. In Figures 5c and 5d, the distribution of velocity dispersion has also enabled us to trace the boundaries of the molecular clouds or the colliding interface (where $\delta V > 2$ km s⁻¹; see a white contour in Figure 5c).

We have further examined the broad bridge feature in E-S235 that contains H II regions. There are many physical processes (such as radiative/mechanical feedback from massive stars) which might act to remove the broad bridge feature in the vicinity of the H II regions. Hence, it seems reasonable to look for the broad bridge features away from the H II regions. Figures 6a, 6b, and 6c show the observed ^{12}CO ($J=1-0$) profiles toward three small areas, reg 1, reg2, and reg 3, respectively (see boxes in Figure 5a). Note that the area, reg 1 is chosen near the boundary of two molecular clouds, while the areas reg 2 and reg 3 are selected near the sites “S235AB” and “S235main”, respectively. Each spectrum is obtained by averaging the area highlighted by the respective box in Figure 5a. Each spectrum shows the previously known two molecular clouds and also reveals a bridge feature seen at the intermediate velocity range that has almost

¹ http://gmrt.ncra.tifr.res.in/gmrt_hpage/Users/doc/obs_manual.pdf

flattened profile. In the star-forming region M20, Torii et al. (2017a) also observed a similar feature in the ^{12}CO spectra (see their Figure 14).

In the velocity space, the existence of a broad bridge feature indicates an observational signature of collisions between molecular clouds (i.e. CCC process; Haworth et al. 2015a,b). Torii et al. (2017a) pointed out that the bridge feature at the intermediate velocity range probes the turbulent motion of the gas enhanced by the collision. They also indicated that the spatially complementary distribution between two clouds is an expected outcome of the CCC and is attributed to identical silhouettes of the smaller cloud and the cavity in the larger cloud projected on the sky (see Figure 1 in Torii et al. 2017a). Based on this argument, we have also examined the channel maps of ^{12}CO and ^{13}CO , and have found a possible complementary pair that appears to be seen in the velocity ranges $[-21, -20]$ km s^{-1} and $[-16, -15]$ km s^{-1} (see Figures 1 and 2).

In Figures 7 and 8, we present the ^{12}CO and ^{13}CO emission contours overlaid on the *Spitzer* 3.6 μm image, respectively. Figures 7a and 8a show the *Spitzer* 3.6 μm image overlaid with the ^{12}CO and ^{13}CO emission integrated over -24 to -18 km s^{-1} , respectively. Figures 7b and 8b present the *Spitzer* 3.6 μm image superimposed with the ^{12}CO and ^{13}CO emission integrated over -18 to -13.5 km s^{-1} , respectively. In Figures 9a and 9b, we show the ^{12}CO and ^{13}CO emission contours overlaid on the *Spitzer* 3.6 μm image, respectively. These emissions are integrated over -18.75 to -17.75 km s^{-1} , which is an intermediate velocity range between two velocity peaks (see Figure 3b). In Figures 7, 8, and 9, we have highlighted previously known different subregions (i.e. East 1, East 2, North, North-West, Central W, Central E, South-West, S235A, S235B, and S235C) and the positions of the ionizing sources within E-S235.

Based on Figures 3c, 4c, 7, 8, and 9, the sites, “S235ABC”, East 1, and South-West subregions are spatially found at the junction of the molecular clouds within E-S235 (also see Section 4 for more details).

3.2. Dust continuum clumps and ionized emission in E-S235

In this section, we study the dust continuum clumps and the distribution of ionized emission in E-S235. The dust continuum map at 1.1 mm allows us to depict the dense and cold regions. Figure 10a shows the gray-scale Bolocam dust continuum map at 1.1 mm overlaid with the dust continuum clumps at 1.1 mm. These clumps were obtained from the Bolocam source catalog v2.1 (Ginsburg et al. 2013). For our selected target region, we find eighteen clumps and fifteen out of them (nos 1-15; see Figure 10a) have been reported in Paper II. These fifteen clumps (i.e. nos 1–15) are distributed toward the “S235main”, while the remaining three clumps (nos 16, 17, and 18) are seen toward the “S235ABC”. In Paper II, the clump masses of first fifteen clumps have been computed which vary between $7 M_{\odot}$ and $285 M_{\odot}$ (see Table 1 in Paper II). The most massive dust clump (i.e. no. 15; $M_{clump} \sim 285 M_{\odot}$) is associated with the East 1 subregion. The mass of a clump seen in the site South-West is reported to be about $60 M_{\odot}$ (see ID #3 in Table 1 in Paper II). Following Paper II, we have also

computed the clump masses of three clumps nos 16, 17, and 18 (see Equation 1 in Paper II for M_{clump}), which are ~ 635 , 70 , and $40 M_{\odot}$, respectively. In the calculation, we have used a dust absorption coefficient ($\kappa_{\nu} = 1.14 \text{ cm}^2 \text{ g}^{-1}$ (e.g. Enoch et al. 2008; Bally et al. 2010), a distance ($D = 1.8$ kpc), and a dust temperature ($T_d = 20$ K (e.g. Kirsanova et al. 2014). A dust clump (i.e. no. 16; $M_{clump} \sim 635 M_{\odot}$) is seen toward the sites S235A and S235B (hereafter “S235AB”). Two clumps (nos 17 and 18; $M_{clump} \sim 40\text{--}70 M_{\odot}$) are found toward the S235C region.

Figure 10b shows an $\text{H}\alpha$ image overlaid with the GMRT 610 MHz emission. Both the images trace the distribution of ionized emission in E-S235. *Spitzer*-IRAC images also show extended bright features in E-S235 and each feature contains the radio continuum emission at its interior (see Figures 7a and 10b). In Figure 10b, we find the spatial match between the $\text{H}\alpha$ emission and the radio continuum emission. The ionized emission is found toward the sites “S235main”, S235A, S235B, and S235C. The “S235main” is powered by a single massive star BD+35°1201 of O9.5V type, while the sites, S235A, S235B, and S235C are linked with the compact H II regions, which are mainly excited by B1V–B0.5V stars (see Table 1 in Bieging et al. 2016). The positions of the ionizing sources are marked in Figure 7a. These results are also in agreement with estimations of Lyman continuum photons using the GMRT 610 MHz data. We have also used the GMRT 610 MHz data to compute the dynamical ages (t_{dyn}) of the H II regions associated with “S235AB” and S235C sites. Adopting a typical value of n_0 (as $10^3(10^4) \text{ cm}^{-3}$), we estimated the dynamical ages of these H II regions to be $\sim 0.06(0.22)$ Myr. In Paper II, the dynamical age (t_{dyn}) of the H II region linked with “S235main” was reported to be ~ 1 Myr. Based on these results, it appears that the H II regions associated with the “S235AB” and S235C sites are relatively younger than the H II region linked with “S235main”.

3.3. Young stellar populations and their clustering

In this section, to probe the star formation activity, we have carried out an investigation of young stellar objects (YSOs) in our selected region. The YSOs are identified using their infrared excess emission which are produced by the envelope and/or the disk of dust around them. Previously, many authors identified the young stellar populations in our selected target (e.g., Allen et al. 2005; Kirsanova et al. 2008; Dewangan & Anandarao 2011; Camargo et al. 2011; Chavarría et al. 2014; Kirsanova et al. 2014; Bieging et al. 2016; Dewangan et al. 2016). In the present work, we have employed the UKIDSS-GPS NIR data for depicting more deeply embedded and faint young stellar populations. It is possible because the UKIDSS-GPS NIR data are three magnitudes deeper than 2MASS. In Paper II, the GPS NIR data were mainly employed for the “S235main” site. Following the analysis presented in Paper II, we have selected sources that have detections only in the H and K bands. To identify infrared excess sources, we have utilized a color-magnitude (H–K/K) diagram (see Figure 11a). The diagram allows to select embedded sources having $\text{H–K} > 1.04$. This color criterion is chosen based on the color-magnitude analysis of a nearby control field (size $\sim 17.6 \times 15.5$;

central coordinates: $\alpha_{J2000} = 05^h43^m35^s.8$, $\delta_{J2000} = +35^\circ20'20''.4$). This condition yields 440 deeply embedded infrared excess sources.

To examine the individual groups or clusters of YSOs in E-S235, the surface density map of YSOs is produced using the nearest-neighbour (NN) technique (also see Gutermuth et al. 2009; Bressert et al. 2010, for more details). We have generated the surface density map of all the selected 440 YSOs, in a manner similar to that utilized in Paper I. The map was obtained using a $5''$ grid and 6 NN at a distance of 1.8 kpc. Figure 11b shows the resultant surface density contours of YSOs overlaid on the dust continuum map at 1.1 mm. The contour levels are shown at 5, 10, 25, and 60 YSOs/pc², increasing from the outer to the inner regions. The figure clearly reveals the spatial correlation between YSOs surface density and dense clumps. The clusters of YSOs are spatially found toward all the subregions/sites, East 1, East 2, North, North-West, Central W, Central E, South-West, S235A, S235B, and S235C (see Figure 11b). In E-S235, this outcome appears in agreement with the work of Chavarría et al. (2014) (also see Figure 21 in Bieging et al. 2016). In Figure 12, we have also overlaid the surface density contours on the molecular ¹³CO emission maps of the redshifted and the blueshifted molecular components. This figure helps us to trace the clustering of YSOs at the junction of two molecular clouds, indicating the intense star formation activities.

4. DISCUSSION

Our present work expands upon the outcomes of Paper II with a more detailed multi-wavelength analysis of E-S235 containing the “S235main” and “S235ABC” sites. In Paper II, the analysis was restricted mainly to the “S235main” site and it was suggested that the star formation activities toward the five subregions (i.e. East 2, North, North-West, Central W, and Central E) could be explained by the expanding H II region via “collect and collapse”. It was also reported that the clusters of YSOs in East 1 subregion might be originated by compression of the pre-existing dense material by the expanding H II region. Furthermore, it was argued that the CCC process might be acting in E-S235. Using the hydrogen radio recombination line observations, Balsler et al. (2011) and Anderson et al. (2015) reported the velocity of the ionized gas to be about -25.6 and -15.3 km s⁻¹ in the H II regions linked with the “S235main” and “S235ABC”, respectively. Considering the velocities of the molecular and ionized gases in E-S235, it is obvious that the molecular cloud linked with the sites “S235ABC” is redshifted relative to the cloud associated with the site “S235main” (also see Figures 7 and 8). Hence, it appears that the molecular cloud containing “S235ABC” is located at the rear side with respect to the “S235main” site. It is in agreement with the CCC scenario. However, a detailed study of the CCC process in E-S235 is still lacking. Hence, considering this interesting possibility, our present analysis has been focused to get more insights of the CCC in E-S235. The CCC process has also been demonstrated in the numerical simulations (see Habe & Ohta 1992; Inoue & Fukui 2013; Takahira et al. 2014; Haworth et al. 2015a,b, and references therein). As mentioned before, the signposts of the CCC are the bridging feature connecting the two

clouds in velocity, the complementary distribution of the two colliding clouds, and broad CO line wing in the intersection of the two clouds. The presence of a broad bridge feature in the velocity space can be interpreted as an evidence of a compressed layer of gas due to the collision between the clouds seen along the line of sight (e.g., Haworth et al. 2015a,b; Torii et al. 2017a,b; Fukui et al. 2017). One can also note that the synthetic observations presented in Haworth et al. (2015a,b) were made with an observer viewing angle parallel to the collisional axis so that the two colliding clouds are spatially coincident along the line of sight. In such a case, two velocity peaks separated by intermediate intensity emissions are found in the velocity space. The same is the case in M20 studied by Torii et al. (2017a). If one observes a CCC with a viewing angle inclined relative to the collisional axis, or if a CCC is an offset collision, the observed position-velocity diagrams and line profiles may be different from those presented in Haworth et al. (2015a,b) and Torii et al. (2017a) (also see Fukui et al. 2017). Using the ¹²CO (J=1-0) and ¹³CO (J=1-0) line data, two molecular clouds are observed in the direction of E-S235 and are interconnected in space as well as in velocity (see Section 3.1). The molecular second momentum map has revealed the colliding interface or the boundaries of the molecular clouds (see Figure 5c). A possible complementary molecular pair at $[-21, -20]$ km s⁻¹ and $[-16, -15]$ km s⁻¹ is also found in E-S235. Furthermore, the existence of the broad bridge feature (see Figures 3c and 4c) and its flattened molecular profiles (see Figure 6) indicate the onset of the CCC process and the presence of the turbulent gas excited by this mechanism. Taken together, all the observed signatures are in agreement with the outcomes of models of the CCC (e.g., Inoue & Fukui 2013; Takahira et al. 2014; Haworth et al. 2015a,b).

In E-S235, we find sites, East 1, “S235ABC”, and South-West seen in the spatially overlapped zones of two molecular clouds (see Figures 5–6 and also Section 3.1). In the sites of the CCC, one may expect the higher values of ratio of CO 3-2/1-0 toward the colliding interface of the colliding clouds (Torii et al. 2015). Bieging et al. (2016) studied E-S235 in CO (2-1), ¹³CO (2-1), and CO (3-2) and presented velocity channel maps of CO (J = 3-2)/(J = 2 -1) intensity ratios, map of velocity dispersion for ¹³CO (2-1), and distribution of CO and ¹³CO (2-1) excitation temperature derived by an LTE model. Using these published results toward the colliding interfaces (i.e. East 1, “S235ABC”, and South-West) in E-S235, the values of CO (J = 3-2)/(J = 2 -1) intensity ratios, velocity dispersion for ¹³CO (2-1), and excitation temperature are found to be about 0.6–0.9, 2–4 km s⁻¹, and 25–40 K, respectively. These values are noticeably high toward the sites, East 1, “S235ABC”, and South-West, and may be explained by the CCC (e.g. Torii et al. 2015, 2017a,b) (also see Figure 5 for the molecular first and second momentum maps in this paper). All these sites are associated with intense star formation activities. The sites, S235A and S235B contain compact H II regions excited by B-type stars. The site East 1 is not associated with any ionized emission and contains many embedded protostars that show outflow activities (see Papers I and II). A massive clump (i.e. $M_{clump} \sim 285 M_{\odot}$) is found toward the East 1. Additionally, this sub-

region is considered as the youngest star-forming site in the S235main (see Kirsanova et al. 2014). In E-S235, the most massive clump (i.e. $M_{clump} \sim 635 M_{\odot}$) is observed toward the sites “S235AB” that have significant gas mass within ~ 2 pc of the clusters. Considering the velocity separation (i.e. $\sim 4 \text{ km s}^{-1}$) of the two colliding clouds in the E-S235, a typical collision timescale is computed to be ~ 0.5 Myr. The dynamical ages of the H II regions associated with the sites “S235AB” are found to be 0.06–0.22 Myr. An average age of the Class I and Class II YSOs is estimated to be ~ 0.44 Myr and ~ 1 –3 Myr, respectively (Evans et al. 2009). Taking into account these timescales, it seems that the formation of youngest populations and massive stars in the interface of two clouds (i.e. East 1, “S235ABC”, and South-West) might be influenced by the CCC about 0.5 Myr ago. However, the stellar populations older than the collision timescale might have formed prior to the collisions of clouds. Hence, we cannot rule out the onset of star formation activities before the collision in E-S235.

Considering the results presented in Paper II and the outcomes of this paper, it reinforces the idea that the E-S235 is a very promising triggered star formation site where the “collect and collapse” (e.g. Kang et al. 2012; Kirsanova et al. 2014; Chavarría et al. 2014; Bieging et al. 2016) and the CCC processes seem to have influenced the star formation activities.

5. SUMMARY AND CONCLUSIONS

In this paper, we have carried out an extensive study of E-S235 (harboring the “S235main” and “S235ABC” sites) using the multi-wavelength data. The major results of our multi-wavelength analysis are the following:

- Using the ^{12}CO ($J=1-0$) and ^{13}CO ($J=1-0$) line data, the molecular gas emission in the direction of E-S235 reveals two noticeable molecular clouds (having velocity peaks at ~ -20.5 and $\sim -16.5 \text{ km s}^{-1}$), which are separated by $\sim 4 \text{ km s}^{-1}$ in the velocity space. The boundaries of the two clouds (or the colliding interface) are traced using the molecular momentum maps. The redshifted molecular component (-18 to -13 km s^{-1}) is linked with the sites S235A, S235B, and S235C, while the blueshifted one (-24 to -18 km s^{-1}) contains the site “S235main”.

- The position-velocity space of ^{12}CO and ^{13}CO depicts a broad bridge feature. In this configuration, the redshifted and the blueshifted molecular components are interconnected by a lower intensity intermediate velocity emission.

- In the velocity channel maps of ^{12}CO and ^{13}CO , a possible complementary molecular pair at $[-21, -20] \text{ km s}^{-1}$ and $[-16, -15] \text{ km s}^{-1}$ is also traced.

- The sites, East 1, “S235ABC”, and South-West are found in the spatially overlapped zones of two molecular clouds.

- Deep UKIDSS NIR photometric analysis of point-like sources gives a total of 440 YSOs in E-S235 and depicts significant clustering of young stellar populations toward the sites located in the interface, and the “S235main”.

- The sites, “S235ABC” harbor young compact H II regions having dynamical ages of ~ 0.06 –0.22 Myr.

- The sites, “S235ABC”, South-West, and East 1 contain dust clumps (having $M_{clump} \sim 40$ to $635 M_{\odot}$).

- A typical collision timescale in E-S235 is estimated to

be ~ 0.5 Myr.

With the observational outcomes presented in this paper, we conclude that the CCC process might have influenced the star formation activities (including massive stars) at the junction about 0.5 Myr ago.

We thank the anonymous reviewers for constructive comments and suggestions which improved the scientific content of this paper. The research work at Physical Research Laboratory is funded by the Department of Space, Government of India. This work is based on data obtained as part of the UKIRT Infrared Deep Sky Survey. This publication made use of data products from the Two Micron All Sky Survey (a joint project of the University of Massachusetts and the Infrared Processing and Analysis Center / California Institute of Technology, funded by NASA and NSF), archival data obtained with the *Spitzer* Space Telescope (operated by the Jet Propulsion Laboratory, California Institute of Technology under a contract with NASA). The Canadian Galactic Plane Survey (CGPS) is a Canadian project with international partners. The Dominion Radio Astrophysical Observatory is operated as a national facility by the National Research Council of Canada. The Five College Radio Astronomy Observatory CO Survey of the Outer Galaxy was supported by NSF grant AST 94-20159. The CGPS is supported by a grant from the Natural Sciences and Engineering Research Council of Canada. The GMRT is run by the National Centre for Radio Astrophysics of the Tata Institute of Fundamental Research. This paper makes use of data obtained as part of the INT Photometric H α Survey of the Northern Galactic Plane (IPHAS, www.iphas.org) carried out at the Isaac Newton Telescope (INT). The INT is operated on the island of La Palma by the Isaac Newton Group in the Spanish Observatorio del Roque de los Muchachos of the Instituto de Astrofísica de Canarias. The IPHAS data are processed by the Cambridge Astronomical Survey Unit, at the Institute of Astronomy in Cambridge.

REFERENCES

- Aguirre, J. E., Ginsburg, A. G., Dunham, M. K., et al. 2011, *ApJS*, 192, 4
- Allen L. E., Hora J. L., Megeath S. T., Deutsch L. K., Fazio G. G., Chavarría L. and Dell R. W. 2005, in Cesaroni R., Felli M., Churchwell E., Walmsley M., eds, *Proc. IAU Symp. 227, Massive star birth: A crossroads of Astrophysics*. Cambridge University Press, Cambridge, p. 352
- Anathpindika, S. V. 2010, *MNRAS*, 405, 1431
- Anderson, L. D., Armentrout, W. P., Johnstone, B. M. et al. 2015, *ApJS*, 221, 26
- Bally, J., Aguirre, J., Battersby, C., et al. 2010, *ApJ*, 721, 137
- Balser, D. S., Rood, R. T., Bania, T. M., & Anderson, L. D. 2011, *ApJ*, 738, 27
- Bieging, J. H., Patel, S., Peters, W. L. et al. 2016, *ApJS*, 226, 13
- Brand, J., & Blitz, L. 1993, *A&A*, 275, 67
- Boley P. A., Sobolev A. M., Krushinsky V. V., van Boekel R., Henning T., Moiseev A. V. and Yushkin M. V. 2009, *MNRAS*, 399, 778
- Bressert, E., Bastian, N., Gutermuth, R., et al. 2010, *MNRAS*, 409, 54
- Brunt C., 2004, in Clemens D., Shah R., Brainerd T., eds, *Proc. of ASP Conference 317. Milky Way Surveys: The Structure and Evolution of our Galaxy*, p. 79
- Burns, R. A., Imai, H., Handa, T., et al. 2015, *MNRAS*, 453, 3163
- Burns, R. A., Handa, T., Hirota, T., et al. 2016, *A&A*, 586, 34

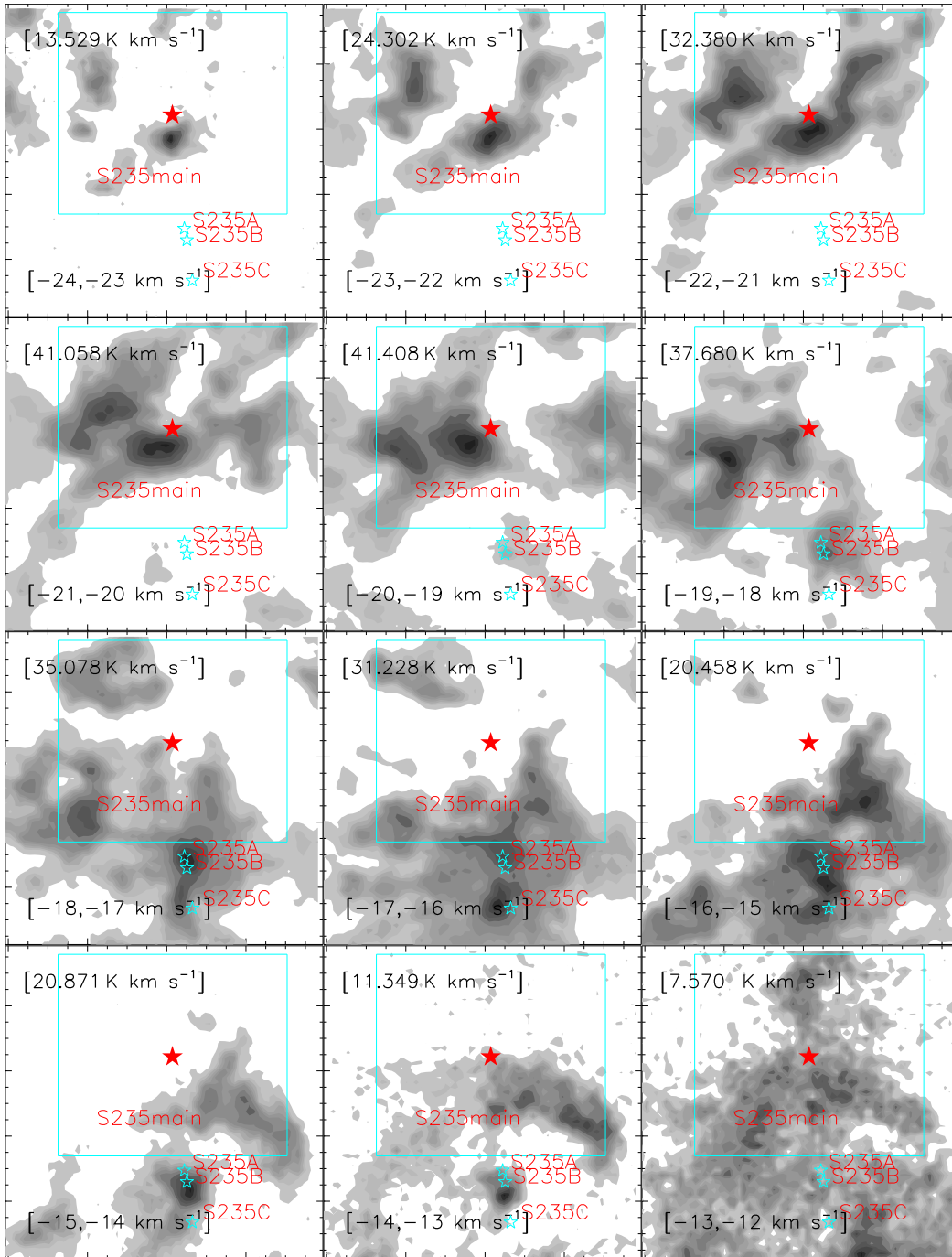


Figure 1. The $^{12}\text{CO}(J=1-0)$ velocity channel contour maps. The molecular emission is integrated over a velocity interval, which is given in each panel (in km s^{-1}). The contour levels are 10, 20, 25, 30, 35, 40, 50, 60, 70, 80, 90, and 98% of the peak value (in K km s^{-1}), which is also provided in each panel. The positions of ionizing stars of S235A, S235B, and S235C are marked by open stars. In the “S235main”, the location of an O9.5V star (BD+35 1201) is highlighted by a filled red star. The solid box shows the area investigated in Paper II which is related to the site “S235main”.

Camargo, D., Bonatto, C., & Bica, E. 2011, 416, 1522
 Chavarría L., Allen L., Brunt C., et al. 2014, MNRAS, 439, 3719
 Dewangan, L. K., & Anandarao, B. G. 2011, MNRAS, 414, 1526
 Dewangan, L. K., Luna, A., Ojha, D. K., et al. 2015, ApJ, 811, 79
 Dewangan, L. K., Ojha, D. K., Luna, A., et al. 2016, ApJ, 819, 66
 Dewangan, L. K. 2017, ApJ, 837, 44
 Drew, J. E., Greimel, R., Irwin, M.J., et al. 2005, MNRAS, 362, 753
 Elmegreen, B. G. & Lada, C. J. 1977, ApJ, 214, 725
 Elmegreen, B. G. 1998, in ASP Conf. Ser. 148, Origins, ed. C. E. Woodward, J. M. Shull, & H. A. Thronson, Jr. (San Francisco, CA: ASP), 150

Enoch, M. L., Evans, II, N. J., Sargent, A. I., et al. 2008, ApJ, 684, 1240
 Evans, N. J., II, & Blair, G. N. 1981, ApJ, 246, 394
 Evans, N. J., II, Beichman, C., Gatley I., et al. 1981, ApJ, 246, 409
 Evans, N. J., II, Dunham, M. M., Jørgensen, J. K., et al. 2009, ApJS, 181, 321
 Felli M., Testi L., Valdetaro R. and Wang J. J. 1997, A&A, 320, 594
 Felli M., Massi F., Navarrini A., Neri R., Cesaroni R. and Jenness T. 2004, A&A, 420, 553

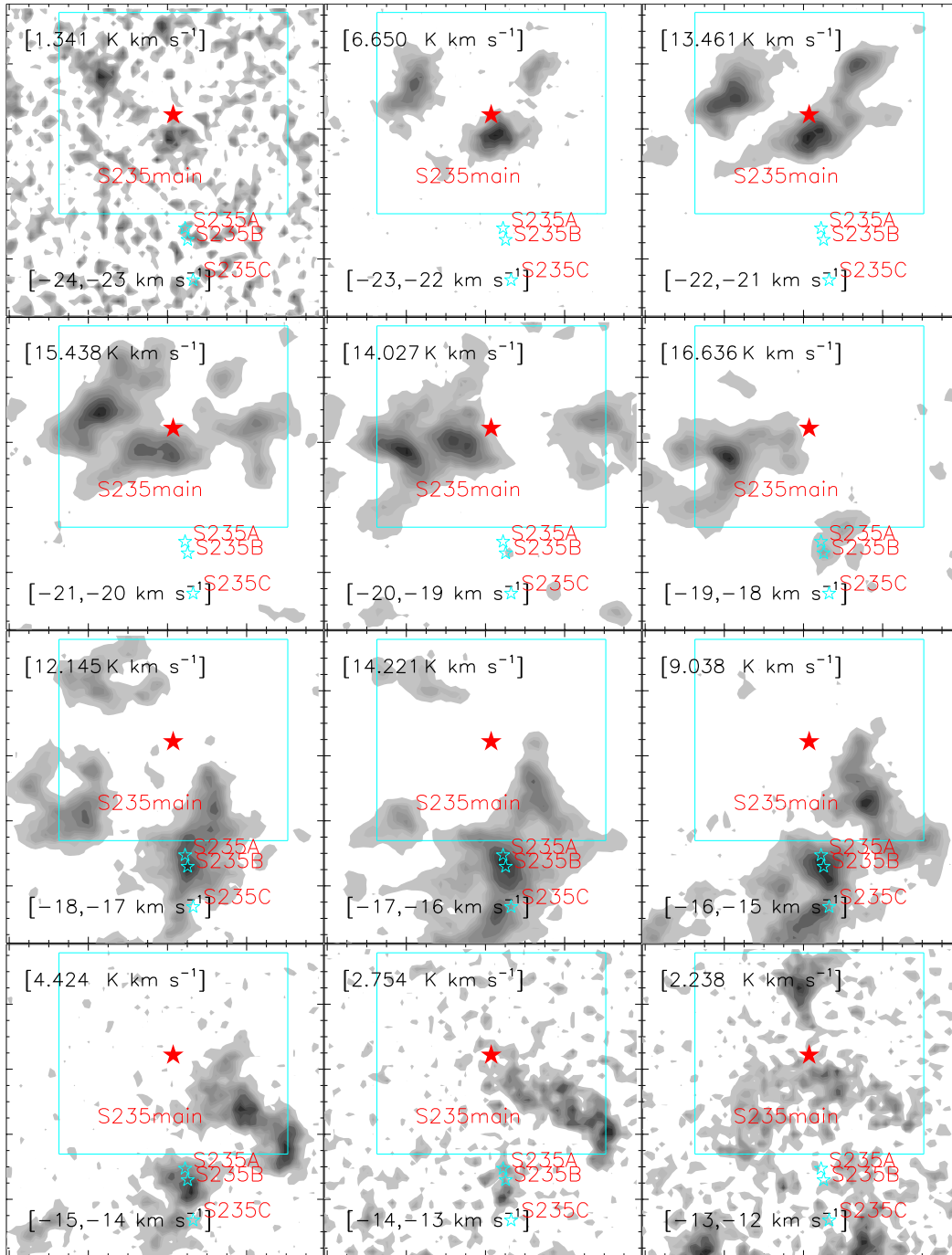


Figure 2. The $^{13}\text{CO}(J=1-0)$ velocity channel contour maps. The molecular emission is integrated over a velocity interval, which is given in each panel (in km s^{-1}). The contour levels are 10, 20, 25, 30, 35, 40, 50, 60, 70, 80, 90, and 98% of the peak value (in K km s^{-1}), which is also provided in each panel. In each panel, other marked symbols and labels are similar to those shown in Figure 1.

Felli M., Massi F., Robberto M. and Cesaroni R. 2006, *A&A*, 453, 911
 Foster, T. & Brunt, C. M. 2015, *AJ*, 150, 147
 Fukui, Y., Ohama, A., Hanaoka, N., et al. 2014, *ApJ*, 780, 36
 Fukui, Y., Torii, K., Ohama, A., et al. 2016, *ApJ*, 820, 26
 Fukui, Y., Kohno, M., Yokoyama, K., et al. 2017, arXiv170605768
 Furukawa, N., Dawson, J. R., Ohama, A., et al. 2009, *ApJL*, 696, L115
 Georgelin, Y. M., Georgelin, Y. P., & Roux S. 1973, *A&A*, 25, 337
 Ginsburg, A., Glenn, J., Rosolowsky, E., et al. 2013, *ApJS*, 208, 14
 Gutermuth, R. A., Megeath, S. T., Myers, P. C., et al. 2009, *ApJS*, 184, 18
 Habe, A., & Ohta, K. 1992, *PASJ*, 44, 203

Haworth, T. J., Tasker, E. J., Fukui, Y., et al. 2015a, *MNRAS*, 450, 10
 Haworth, T. J., Shima, K., Tasker, E. J., et al. 2015b, *MNRAS*, 454, 1634
 Heyer, M. H., Carpenter, J. M., & Ladd, E. F. 1996, *ApJ*, 463, 630
 Heyer, M., Brunt, C., Snell, R., et al. 1998, *ApJS*, 115, 241
 Inoue, T., & Fukui, Y. 2013, *ApJL*, 774, 31
 Israel, F. P., & Felli, M. 1978, *A&A*, 63, 325
 Kang, J., Koo, B., & Salter, C. 2012, *AJ*, 143, 75
 Kirsanova, M. S., Sobolev, A. M., Thomasson, M., et al. 2008, *MNRAS*, 388, 729
 Kirsanova, M. S., Wiebe, D. S., Sobolev, A. M., et al. 2014, *MNRAS*, 437, 1593

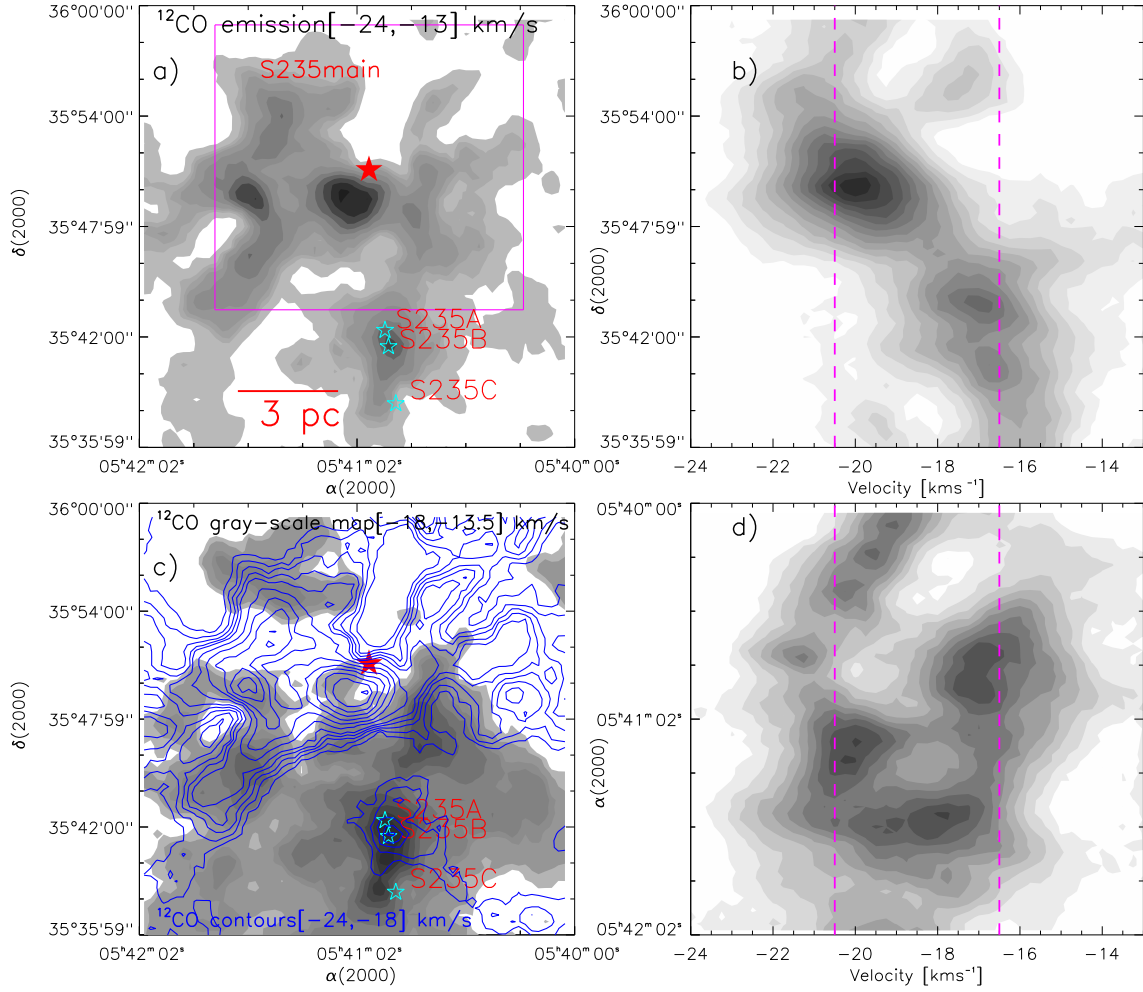


Figure 3. The distribution of molecular gas toward E-S235 (including “S235main” and “S235ABC”). a) Integrated intensity map of ^{12}CO ($J = 1-0$) from -24 to -13 km s^{-1} . The contour levels are 20, 30, 35, 40, 50, 60, 70, 80, 90, and 98% of the peak value (i.e. 130.929 K km s^{-1}). b) Declination-velocity map of ^{12}CO . The ^{12}CO emission is integrated over the right ascension range from $05^{\text{h}}42^{\text{m}}02^{\text{s}}$ to $05^{\text{h}}40^{\text{m}}00^{\text{s}}$. c) Two molecular components (a redshifted and a blueshifted) in the direction of E-S235. The ^{12}CO emission contours from -24 to -18 km s^{-1} are overlaid on the ^{12}CO emission map. The background ^{12}CO emission map (from -18 to -13.5 km s^{-1}) is shown with levels of 79.628 $\text{K km s}^{-1} \times (0.1, 0.15, 0.25, 0.3, 0.4, 0.5, 0.6, 0.7, 0.8, 0.9, \text{ and } 0.98)$. The ^{12}CO contours (in blue) are shown with levels of 121.6 $\text{K km s}^{-1} \times (0.1, 0.15, 0.2, 0.3, 0.45, 0.5, 0.6, 0.7, 0.8, 0.9, \text{ and } 0.98)$. d) Right Ascension-velocity map of ^{12}CO . The ^{12}CO emission is integrated over the declination range from $+35^{\circ}35'59''$ to $+36^{\circ}00'00''$. In both the left panels (i.e. Figures 3a and 3c), the marked symbols are similar to those shown in Figure 1. There are two velocity peaks (a blueshifted at ~ -20.5 km s^{-1} and a redshifted at ~ -16.5 km s^{-1}) seen in the position-velocity maps (i.e. Figures 3b and 3d) which are highlighted by dashed magenta lines. These peaks are separated by a lower intensity intermediate velocity emission (i.e., a broad bridge feature; also see the text).

Ladeyschikov, D. A., Kirsanova, M. S., Tsivilev, A. P., & Sobolev, A. M. 2016, *AstBu*, 71, 208
 Lawrence, A., Warren, S. J., Almaini, O., et al. 2007, *MNRAS*, 379, 1599
 Mallick, K. K., Kumar, M. S. N., Ojha, D. K., et al. 2013, *ApJ*, 779, 113
 Navarete, F., Daminieli, A., Barbosa, C. L., & Blum, R. D. 2015, *MNRAS*, 450, 4364
 Nordh, H. L., van Duinen, R. J., Fridlund, C. V. M., et al. 1984, *A&A*, 131, 221

Ohama, A., Dawson, J. R., Furukawa, N., et al. 2010, *ApJ*, 709, 975
 Preibisch, T. & Zinnecker, H., 2007, in Elmegreen B. G., Palous J., eds, *Proc. IAU Symp. 237, Triggered Star Formation in a Turbulent ISM*. Cambridge Univ. Press, Cambridge, p. 270
 Skrutskie, M. F., Cutri, R. M., Stiening, R., et al. 2006, *AJ*, 131, 1163
 Takahira, K., Tasker, E. J., & Habe, A. 2014, *ApJ*, 792, 63
 Torii, K., Hasegawa, K., Hattori, Y., et al. 2015, *ApJ*, 806, 7
 Torii, K., Hattori, Y., Hasegawa, K., et al. 2017a, *ApJ*, 835, 142
 Torii, K., Hattori, Y., Matsuo, M., et al. 2017b, *arXiv170607164*

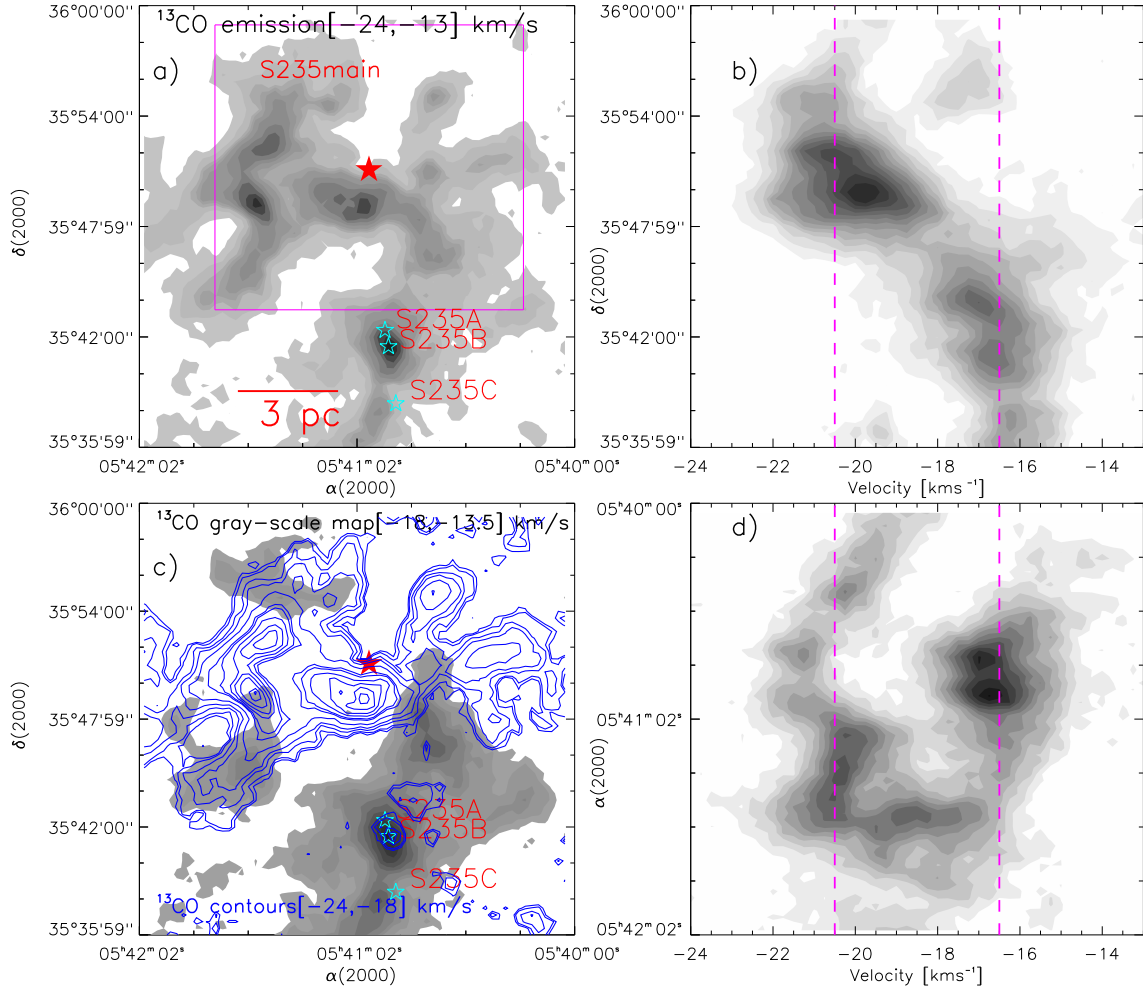


Figure 4. The distribution of molecular gas toward E-S235 (including “S235main” and “S235ABC”). a) Integrated intensity map of ^{13}CO ($J = 1-0$) from -24 to -13 km s^{-1} . The contour levels are 10, 20, 30, 35, 40, 50, 60, 70, 80, 90, and 98% of the peak value (i.e. 36.046 K km s^{-1}). b) Declination-velocity map of ^{13}CO . The ^{13}CO emission is integrated over the right ascension range from $05^{\text{h}}42^{\text{m}}02^{\text{s}}$ to $05^{\text{h}}40^{\text{m}}00^{\text{s}}$. c) Two molecular components (a redshifted and a blueshifted) in the direction of E-S235. The ^{13}CO emission contours from -24 to -18 km s^{-1} are overlotted on the ^{13}CO emission map. The background ^{13}CO emission map (from -18 to -13.5 km s^{-1}) is shown with levels of 31.587 $\text{K km s}^{-1} \times (0.09, 0.15, 0.25, 0.3, 0.4, 0.5, 0.6, 0.7, 0.8, 0.9, \text{ and } 0.98)$. The ^{13}CO contours (in blue) are shown with levels of 32.252 $\text{K km s}^{-1} \times (0.08, 0.1, 0.15, 0.2, 0.3, 0.45, 0.5, 0.6, 0.7, 0.8, 0.9, \text{ and } 0.98)$. d) Right Ascension-velocity map of ^{13}CO . The ^{13}CO emission is integrated over the declination range from $+35^{\circ}35'59''$ to $+36^{\circ}00'00''$. In both the left panels (i.e. Figures 4a and 4c), the marked symbols are similar to those shown in Figure 1. There are two velocity peaks (a blueshifted at ~ -20.5 km s^{-1} and a redshifted at ~ -16.5 km s^{-1}) seen in the position-velocity maps (i.e. Figures 4b and 4d) which are highlighted by dashed magenta lines. These peaks are separated by a lower intensity intermediate velocity emission (i.e., a broad bridge feature; also see the text).

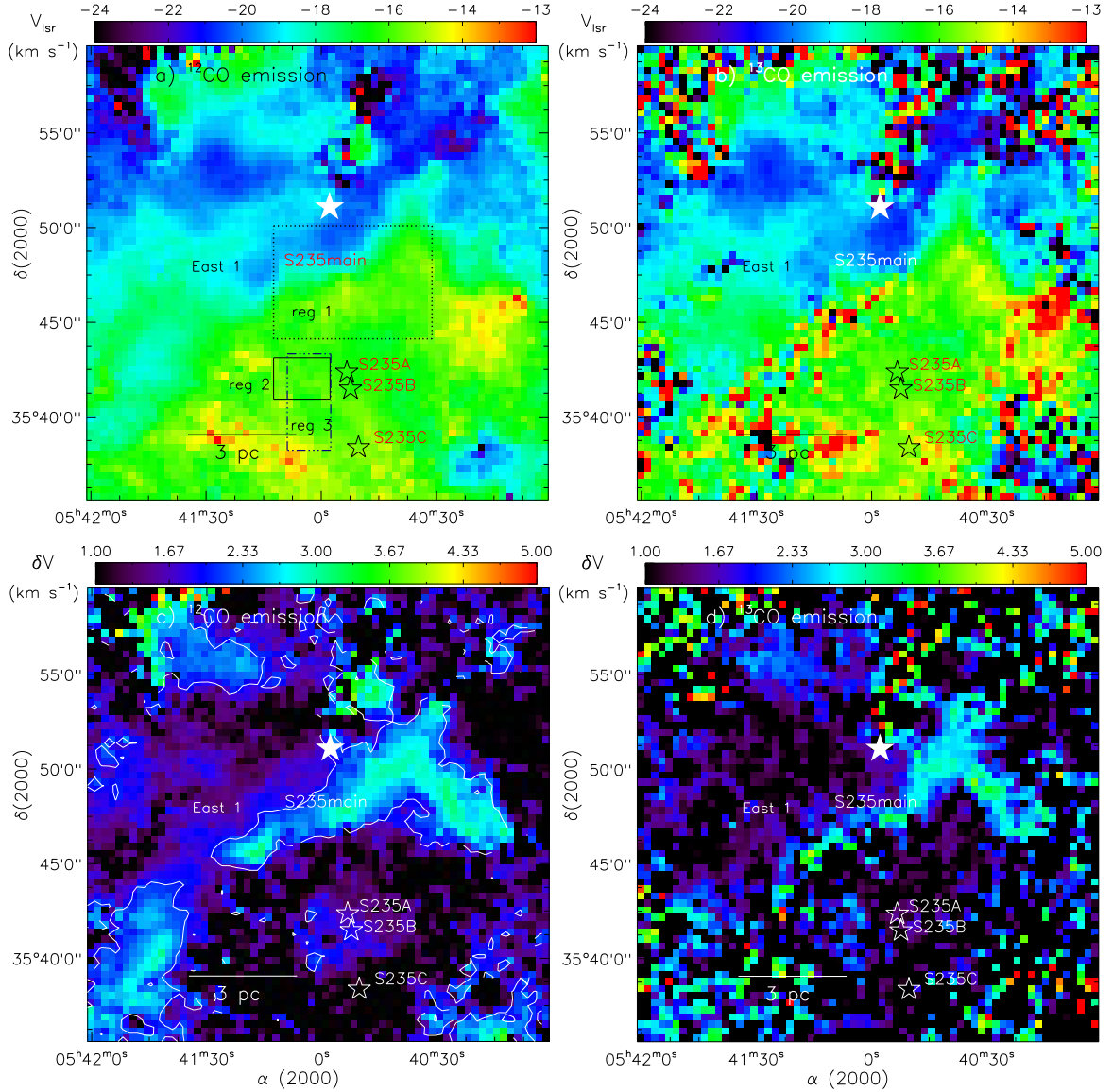


Figure 5. a) ^{12}CO first momentum map. Three small areas (i.e. reg 1, reg 2, and reg 3) are also highlighted by boxes in the figure. b) ^{13}CO first momentum map. c) ^{12}CO second momentum map (i.e. velocity dispersion (δV)). A velocity dispersion contour (in white) is also shown with a level of 2 km s^{-1} . d) ^{13}CO second momentum map. In each top panel, the bar at the top shows the color-coded V_{lsr} in km s^{-1} (see Figures 5a and 5b). In each bottom panel, the bar at the top shows the color-coded δV in km s^{-1} (see Figures 5c and 5d). In all the panels, the marked symbols are similar to those shown in Figure 3a.

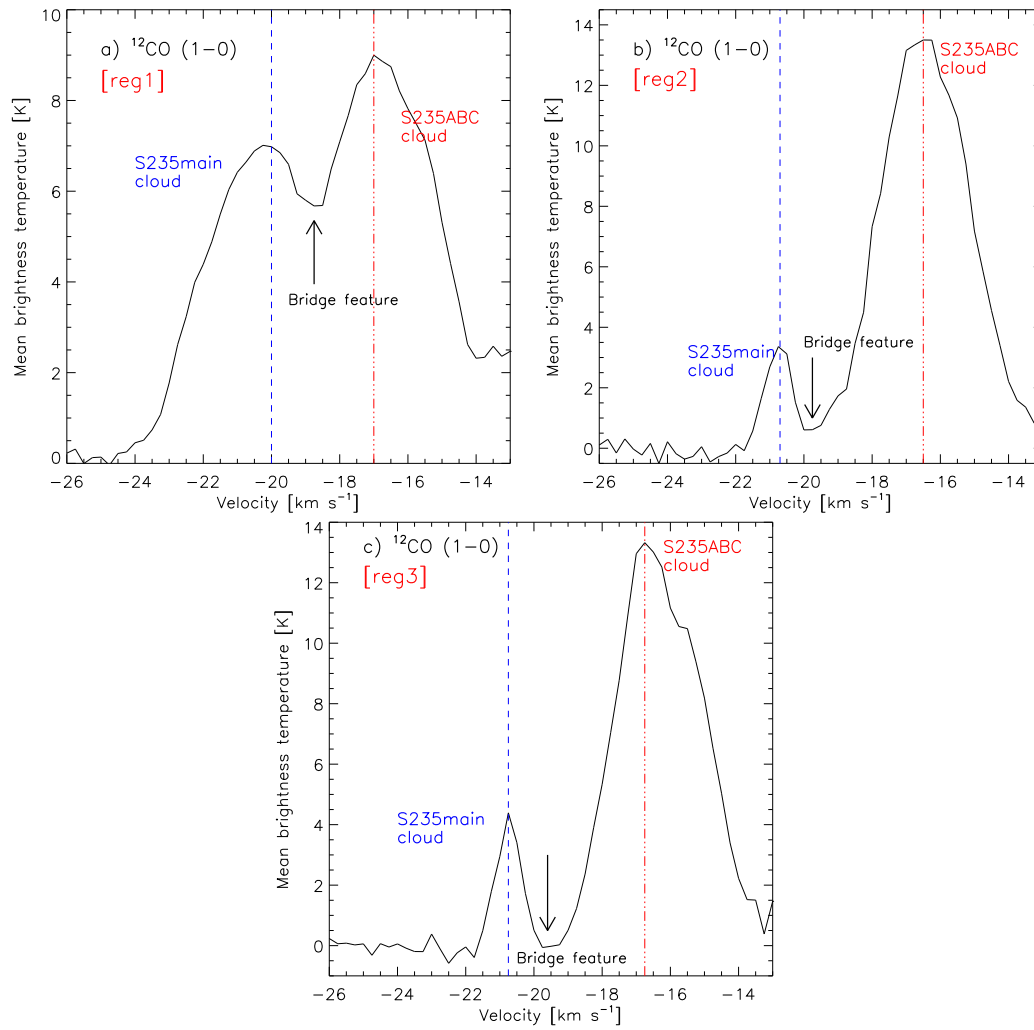


Figure 6. ^{12}CO (1-0) spectra toward our selected three small areas (i.e. reg 1, reg 2, and reg 3; see highlighted boxes in Figure 5a). Each spectrum is obtained by averaging each area. In each spectrum, an almost flattened profile is seen between two velocity peaks (i.e. a bridge feature at the intermediate velocity range).

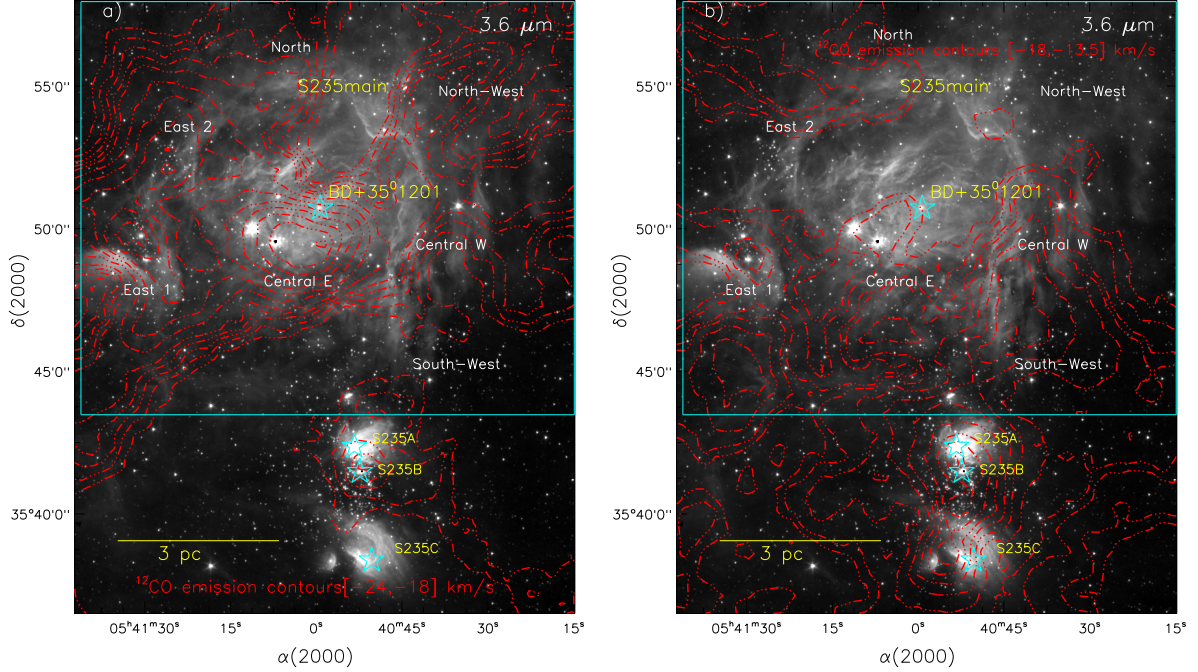


Figure 7. a) *Spitzer* 3.6 μm image is overlaid with the ^{12}CO emission integrated over -24 to -18 km s^{-1} . b) *Spitzer* 3.6 μm image is overlaid with the ^{12}CO emission integrated over -18 to -13.5 km s^{-1} . In both the panels, different subregions are labeled (also see Figure 1 in Dewangan et al. 2016). The scale bar on the bottom left shows a size of 3 pc at a distance of 1.8 kpc in each panel. In each panel, the contours are similar to the one shown in Figure 3c. In both the panels, the positions of ionizing stars of “S235main”, S235A, S235B, and S235C are also highlighted by open stars (also see Table 1 in Bieging et al. 2016). The positions of ionizing stars of S235A, S235B, and S235C are marked by open stars. In each panel, a solid box shows the area investigated in Paper II.

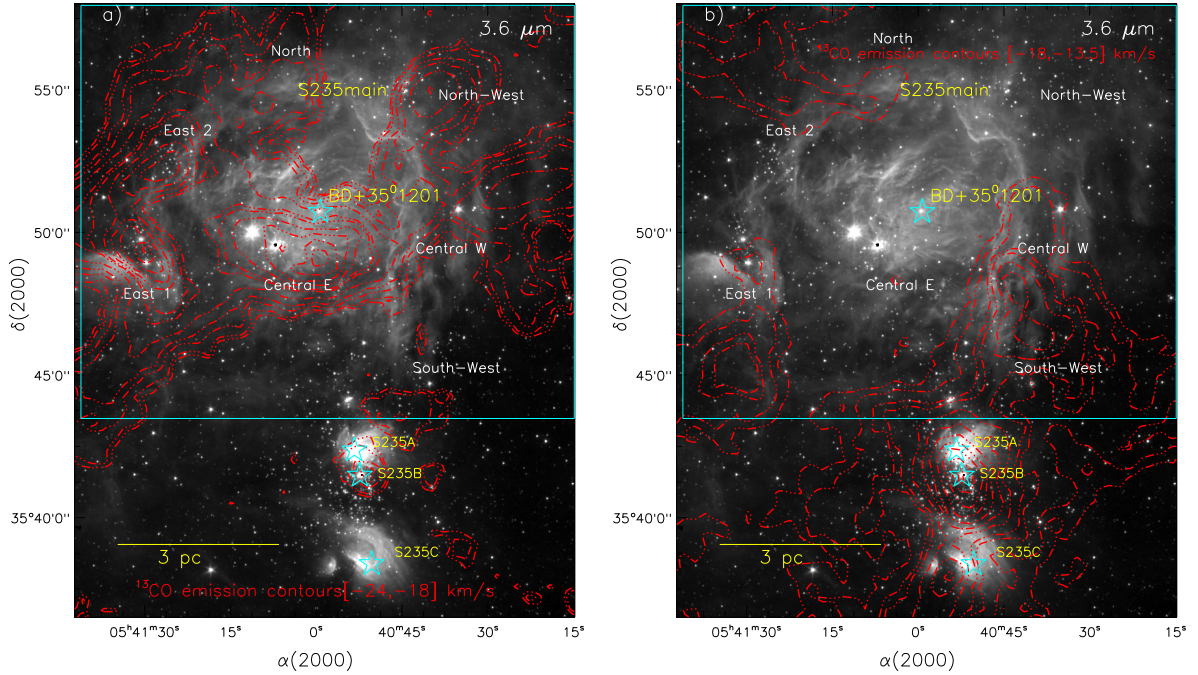


Figure 8. a) *Spitzer* 3.6 μm image is overlaid with the ^{13}CO emission integrated over -24 to -18 km s^{-1} . b) *Spitzer* 3.6 μm image is overlaid with the ^{13}CO emission integrated over -18 to -13.5 km s^{-1} . In both the panels, different subregions are labeled (also see Figure 1 in Dewangan et al. 2016). The scale bar on the bottom left shows a size of 3 pc at a distance of 1.8 kpc in each panel. In each panel, the contours are similar to the one shown in Figure 4c. In each panel, other marked symbols and labels are similar to those shown in Figure 7a.

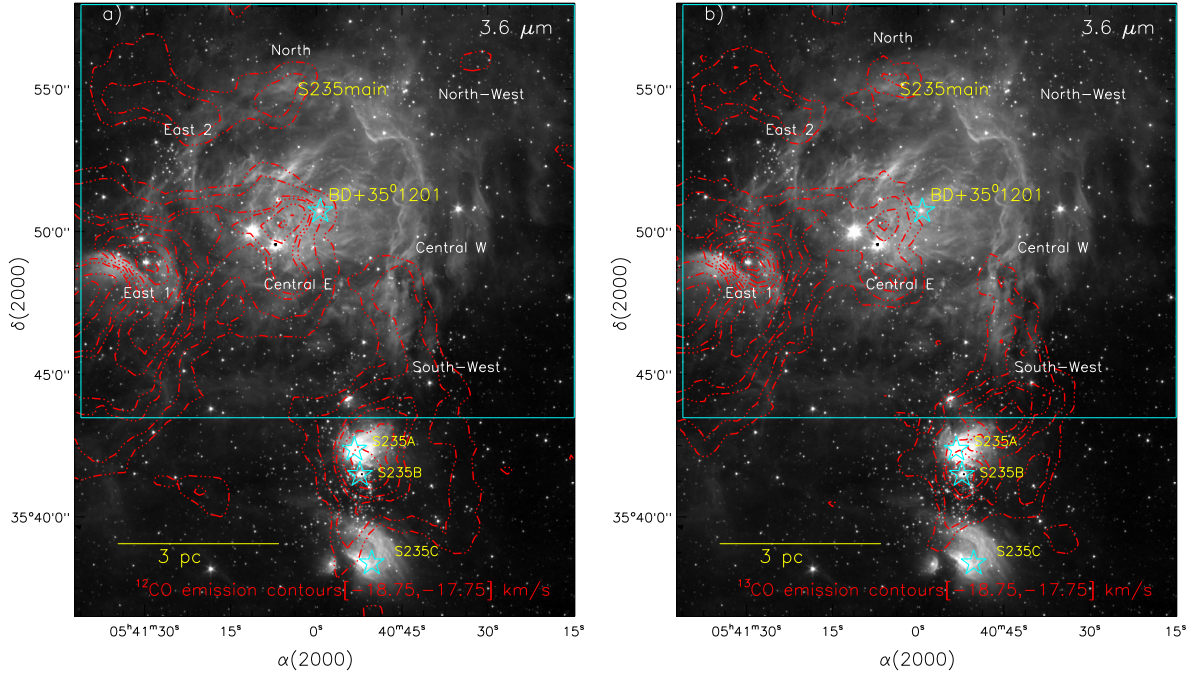


Figure 9. a) *Spitzer* 3.6 μm image is overlaid with the ^{12}CO emission integrated over -18.75 to -17.75 km s^{-1} . The ^{12}CO contours are shown with levels of $35.933 \text{ K km s}^{-1} \times (0.2, 0.3, 0.45, 0.5, 0.6, 0.7, 0.8, 0.9, \text{ and } 0.98)$. b) *Spitzer* 3.6 μm image is overlaid with the ^{13}CO emission integrated over -18.75 to -17.75 km s^{-1} . The ^{13}CO contours are shown with levels of $14.402 \text{ K km s}^{-1} \times (0.09, 0.15, 0.25, 0.3, 0.4, 0.5, 0.6, 0.7, 0.8, 0.9, \text{ and } 0.98)$. In both the panels, different subregions are labeled (also see Figure 1 in Dewangan et al. 2016). The scale bar on the bottom left shows a size of 3 pc at a distance of 1.8 kpc in each panel. In each panel, other marked symbols and labels are similar to those shown in Figure 7a.

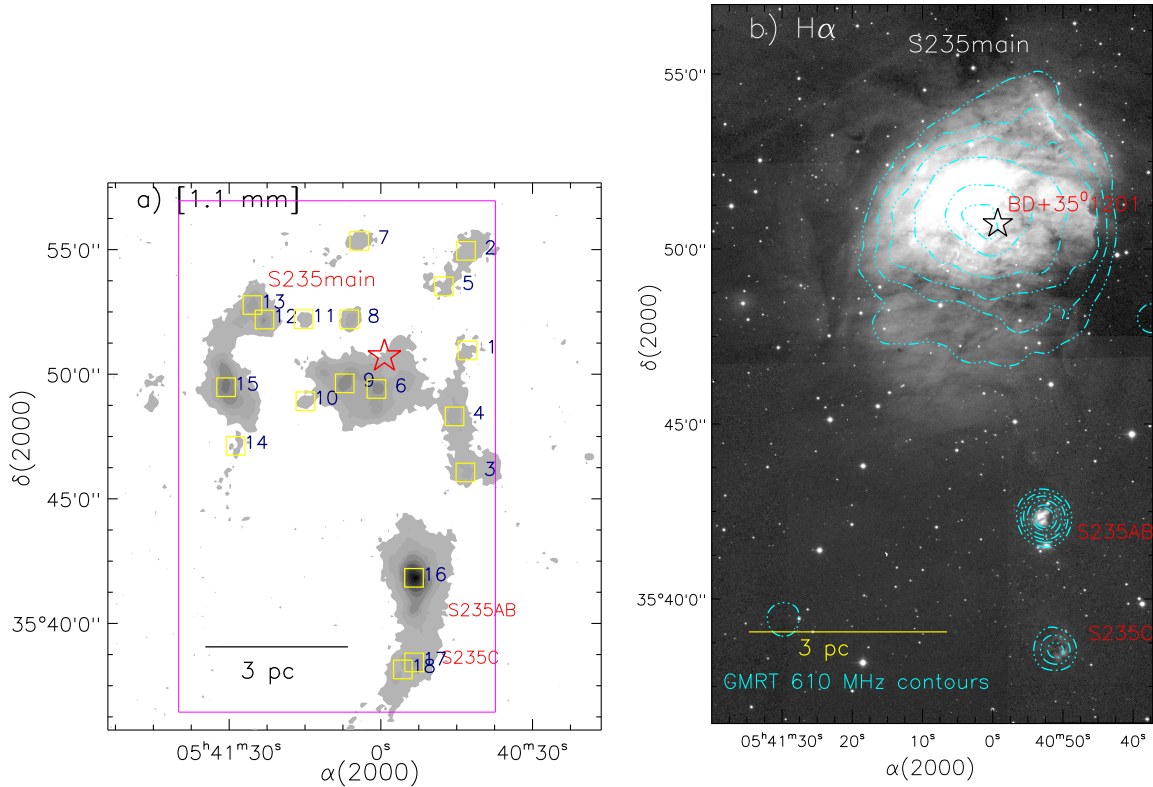


Figure 10. a) Bolocam 1.1 mm dust continuum contour map (beam size $\sim 33''$) of E-S235. The contour levels are 2.5, 8, 15, 20, 30, 40, 55, 70, 85, and 95% of the peak value i.e. 3.39 Jy/beam. The positions of dust clumps at 1.1 mm are highlighted by yellow squares and are also labeled. The clump nos 1–15 are distributed toward the “S235main” (also see Paper II), while the clump nos 16–18 are found toward the “S235ABC”. The solid magenta box encompasses the area shown in Figure 10b. b) IPHAS H α gray-scale image is overlaid with the GMRT 610 MHz emission contours. The GMRT 610 MHz dotted-dashed contours (in cyan) are shown with levels of 0.01, 0.024, 0.04, 0.07, 0.12, and 0.15 Jy/beam. In both the panels, other marked symbols and labels are similar to those shown in Figure 7a.

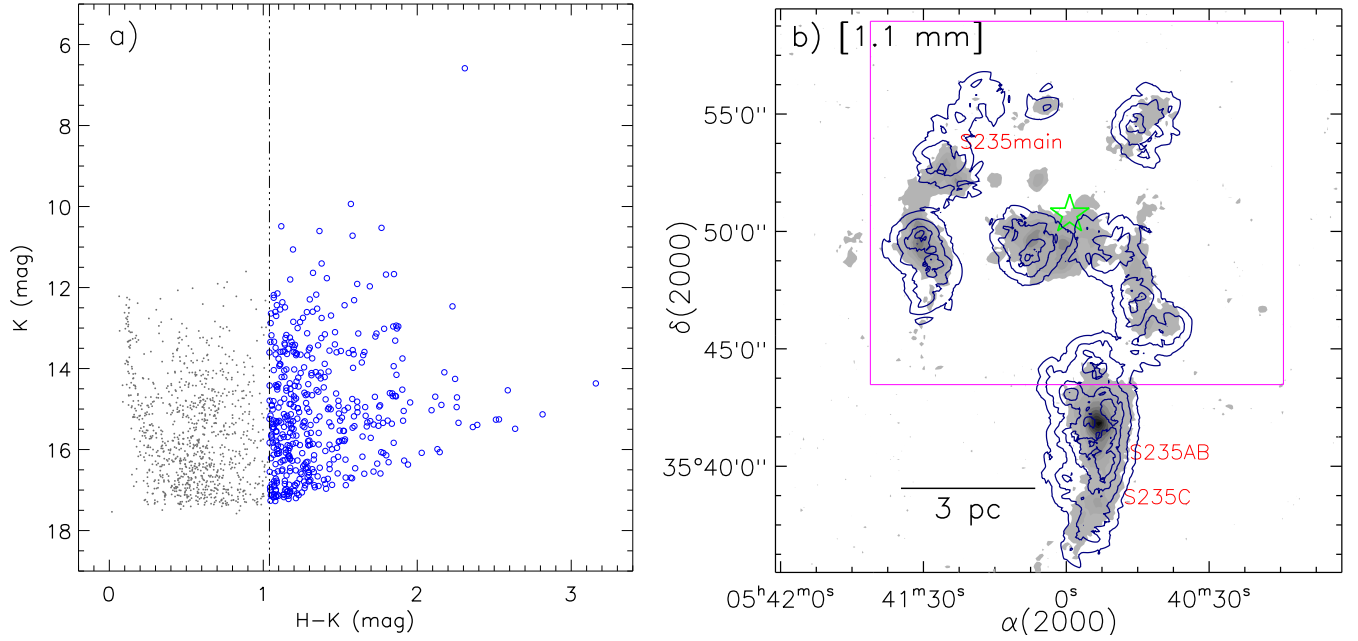


Figure 11. a) Selection of embedded young stellar populations within E-S235. The GPS-2MASS color-magnitude diagram (H-K/K) of the sources detected in H and K bands. The identified YSOs are marked by open blue circles, while the dots in gray color refer the stars with only photospheric emissions. In the NIR H-K/K plot, we have plotted only 1001 out of 5401 stars with photospheric emissions. Due to large numbers of stars with photospheric emissions, only some of these stars are randomly shown in the NIR H-K/K plot. A dotted-dashed line separates the identified YSOs against the stars with photospheric emissions. b) The surface density contours (in navy) of all the identified YSOs are overlaid on the 1.1 mm dust continuum map. The background map is similar to the one shown in Figure 10a. The contours are shown at 5, 10, 25, and 60 YSOs/pc², from the outer to the inner side. A solid box shows the area investigated in Paper II. Other marked symbol and labels are similar to those shown in Figure 7a.

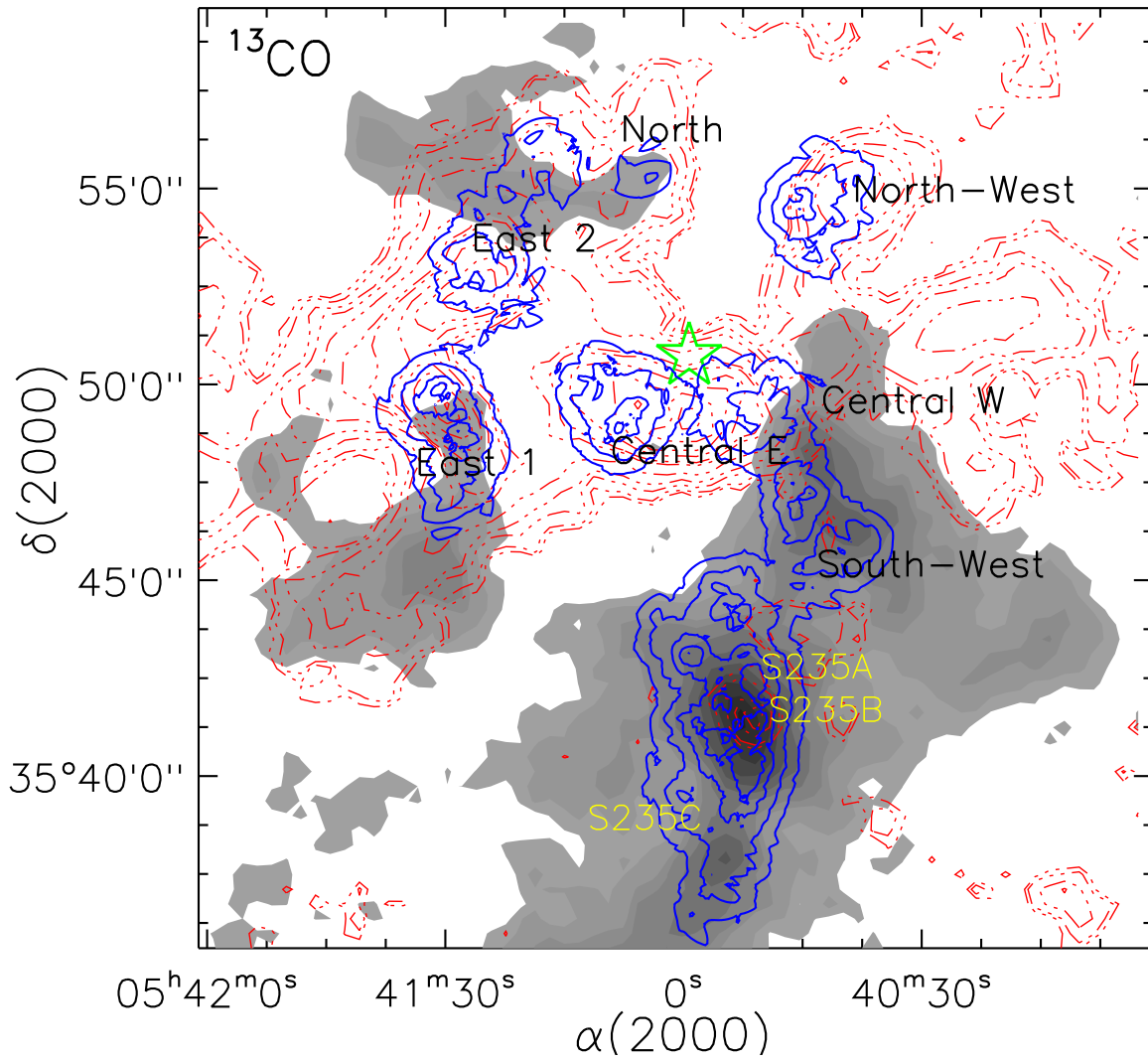


Figure 12. The surface density contours (in blue) of all the identified YSOs are overlaid on the molecular ^{13}CO maps. The background maps are similar to the one shown in Figure 4c. The surface density contours are shown at 5, 10, 25, and 60 YSOs/pc², from the outer to the inner side. Other marked symbol and labels are similar to those shown in Figure 7a.